

The observed sensitivity of high clouds to mean surface temperature anomalies in the tropics

Mark D. Zelinka^{1,2} and Dennis L. Hartmann¹

Received 23 June 2011; revised 9 September 2011; accepted 28 September 2011; published 2 December 2011.

[1] Cloud feedback represents the source of largest diversity in projections of future warming. Observational constraints on both the sign and magnitude of the feedback are limited, since it is unclear how the natural variability that can be observed is related to secular climate change, and analyses have rarely been focused on testable physical theories for how clouds should respond to climate change. In this study we use observations from a suite of satellite instruments to assess the sensitivity of tropical high clouds to interannual tropical mean surface temperature anomalies. We relate cloud changes to a physical governing mechanism that is sensitive to the vertical structure of warming. Specifically, we demonstrate that the mean and interannual variability in both the altitude and fractional coverage of tropical high clouds as measured by CloudSat, the Moderate Resolution Imaging Spectroradiometer, the Atmospheric Infrared Sounder, and the International Satellite Cloud Climatology Project are well diagnosed by upper tropospheric convergence computed from the mass and energy budget of the clear-sky atmosphere. Observed high clouds rise approximately isothermally in accordance with theory and exhibit an overall reduction in coverage when the tropics warms, similar to their behavior in global warming simulations. Such cloud changes cause absorbed solar radiation to increase more than does outgoing longwave radiation, resulting in a positive but statistically insignificant net high cloud feedback in response to El Niño–Southern Oscillation. The results suggest that the convergence metric based on simple mass and energy budget constraints may be a powerful tool for understanding observed and modeled high cloud behavior and for evaluating the realism of modeled high cloud changes in response to a variety of forcings.

Citation: Zelinka, M. D., and D. L. Hartmann (2011), The observed sensitivity of high clouds to mean surface temperature anomalies in the tropics, *J. Geophys. Res.*, 116, D23103, doi:10.1029/2011JD016459.

1. Introduction

[2] The role of cloud-induced changes in top of atmosphere radiative fluxes as a feedback on a warming climate is a subject of great debate and uncertainty [e.g., *Bony et al.*, 2006]. The magnitude of cloud feedback is generally positive in global climate models (GCMs), but exhibits considerable intermodel spread that arises primarily from the spread in shortwave (SW) cloud feedbacks that can be attributed to the wide range of modeled responses of subtropical marine boundary layer clouds [e.g., *Bony and Dufresne*, 2005]. Although most of the spread in estimates of climate sensitivity from GCMs can be attributed to the inter-model variance in SW cloud feedback, *Zelinka and Hartmann* [2010] (hereafter ZH10), showed that the longwave (LW) cloud feedback is robustly positive in twelve

GCMs integrated under the Special Report on Emission Scenarios (SRES) A2 emissions scenario and submitted to the Coupled Model Intercomparison Project phase 3 (CMIP3) multimodel database. They estimated that the tendency for tropical high clouds to rise as the climate warms contributes $0.5 \text{ W m}^{-2} \text{ K}^{-1}$ to the global mean LW cloud feedback, making it robustly positive. Furthermore, they demonstrated that the radiatively driven clear-sky diabatic convergence, whose peak corresponds closely with the level of peak convective detrainment and abundant high cloudiness, provides a useful tool for accurately diagnosing the upward shift in cloud fraction in all of the CMIP3 GCMs analyzed. The robust nature of the positive LW cloud feedback, therefore, arises simply as a fundamental result of the approximate radiative-convective equilibrium that any model must maintain in the tropics regardless of the details of its convection scheme. However, unlike the isothermal upward shift of high clouds expected from the fixed anvil temperature (FAT) hypothesis of *Hartmann and Larson* [2002], ZH10 found that the peak clear-sky radiatively driven convergence and attendant high clouds warmed slightly in the A2 simulations, a feature they referred to as the proportionately higher anvil temperature (PHAT).

¹Department of Atmospheric Sciences, University of Washington, Seattle, Washington, USA.

²Program for Climate Model Diagnosis and Intercomparison, Lawrence Livermore National Laboratory, Livermore, California, USA.

[3] Considering that climate models include a convective parameterization that adjusts toward radiative-convective equilibrium, it is perhaps not surprising that the tropical mass and energy balance is effective at diagnosing the altitude of peak modeled high cloud coverage. Nevertheless, *Kubar et al.* [2007] demonstrated the close relationship between clear sky convergence and high cloud fraction measured by the Moderate Resolution Imaging Spectroradiometer (MODIS) in three regions of the Pacific Intertropical Convergence Zone (ITCZ), indicating that the real atmosphere is also reasonably explained by an assumption of radiative-convective balance. Still, it is unclear on what spatial and temporal scales the constraints imposed by this balance are most applicable. Convection responds quickly to variations in temperature and humidity in its near vicinity, and by moistening the near environment convection can improve the conditions for its own existence, aggregate, and achieve higher altitudes. Furthermore, organized large-scale motion can cool the air adiabatically and provide for deeper convection. For convection to continue, however, radiation must destabilize the vertical profile of temperature diabatically, and this becomes an inefficient process at low temperatures in the upper tropical troposphere, where the saturation vapor pressure is very low and water vapor becomes a less effective emitter [*Hartmann et al.*, 2001a].

[4] In contrast to the lack of sensitivity of tropical high cloud top temperatures to surface temperature (T_{sfc}) changes expected from the FAT hypothesis, *Chae and Sherwood* [2010] showed that cloud top temperatures observed by the Multiangle Imaging Spectroradiometer (MISR) exhibit appreciable seasonal fluctuations (~ 5 K) that are associated with lapse rate changes in the upper troposphere. This study looked at a limited domain rather than at the cloud properties of the entire tropics; thus it remains unclear whether tropical cloud fields exhibit compensatory changes in structure that result in minimal changes when integrated over the entire tropics. Indeed, *Xu et al.* [2005, 2007] and *Eitzen et al.* [2009] demonstrated that the distribution of tropical high cloud top temperatures remains qualitatively unchanged across significantly different SST distributions. These studies did not attempt to show consistency between high clouds and the radiatively driven clear-sky convergence, however, which would have put the cloud response on more solid theoretical footing. Thus, the small body of literature that exists on the distribution of cloud top temperatures is equivocal with regard to FAT, and has not yet been assessed in light of PHAT, which accounts for changes in static stability that affect cloud top temperature.

[5] The change in the altitude of peak cloudiness with underlying temperature is not the only aspect of high cloud changes with relevance for cloud feedback that has been investigated observationally. *Lindzen et al.* [2001] presented results that implied a decrease in cirrus detrainment from deep convective cores as SSTs increase (the adaptive iris hypothesis), which the authors hypothesized was due to increasing precipitation efficiency in convection over warmer waters. The vigorous debate in the literature that continues to the present casts doubt on the robustness of the results [e.g., *Harrison*, 2002; *Hartmann and Michelsen*, 2002a, 2002b; *Del Genio and Kovari*, 2002; *Lin et al.*, 2002; *Chambers et al.*, 2002; *Rapp et al.*, 2005; *Lin et al.*, 2006; *Su et al.*, 2008]. However, neither the iris paper nor

the responses it spawned have utilized the clear-sky diagnostics that operate on a gross tropicswide scale to explain changes in high clouds in observations. Rather, all have attempted to link cloud properties to the underlying SSTs, which we argue offers a weak constraint on high cloud properties and thus makes it difficult to draw conclusions relevant to a warming climate.

[6] In this study we assess the degree to which the distribution of tropical cloud tops as measured by a suite of satellite instruments changes in a manner consistent with that predicted by the clear-sky energy budget as the tropics warms and cools. We focus primarily on the period September 2002 through July 2010, for which a wealth of satellite information is available from A-Train instruments, but also make use of the longer cloud record from the International Satellite Cloud Climatology Project (ISCCP) that extends back to July 1983. Additionally, information about the height and optical depth of clouds from MODIS and ISCCP will be used in conjunction with a radiative transfer model to estimate the impact of interannual cloud fluctuations on the top-of-atmosphere (TOA) energy budget.

[7] We wish to stress that our analysis is not predicated on the assumption that cloud fluctuations associated with El Niño–Southern Oscillation (ENSO) are surrogates for those accompanying global warming forced by increased greenhouse gas concentrations. Rather, we demonstrate that a metric based on fundamental principles of saturation vapor pressure, radiative transfer, and mass and energy balance accurately diagnoses the vertical structure of tropical high clouds and its fluctuations observed in nature, just as it does in global warming simulations of GCMs (ZH10) and in cloud resolving model experiments of *Kuang and Hartmann* [2007] and B. E. Harrop and D. L. Hartmann (Testing the role of radiation in determining tropical cloud top temperature, submitted to *Journal of Climate*, 2011). The observational results presented here reinforce the value of this diagnostic tool for understanding the varied response of high clouds to different forcings operating across time scales and for evaluating modeled tropical high cloud changes and their implied feedbacks.

2. Data

[8] We have chosen to analyze data from a suite of satellite instruments because each instrument has strengths and weaknesses, and a common signal found in several independent data sets can be considered more reliable and robust. Our analysis is restricted to the tropics, defined as the region equatorward of 30° .

2.1. Atmospheric Infrared Sounder

[9] The Atmospheric Infrared Sounder (AIRS) onboard Aqua is actually several instruments: a hyperspectral infrared instrument (i.e., AIRS), the Advanced Microwave Sounding Unit A (AMSU-A), and a visible and near-IR sensor [*Aumann et al.*, 2003]. The AIRS retrieval algorithm makes use of a novel cloud clearing technique that exploits the relative insensitivity of microwave temperature measurements to the presence of clouds, allowing retrievals to be made in the presence of up to 70% cloud cover [*Aumann et al.*, 2003; *Susskind et al.*, 2003]. Cloud fraction reported by AIRS is actually the product of geometric cloud fractional

coverage and its emissivity at 11 μm . The effective cloud fraction and cloud top pressure are retrieved by comparison of the observed AIRS radiance with a cloud radiance computed using surface and atmospheric properties derived from the clear column radiances.

[10] We use retrievals of cloud fraction, water vapor mixing ratio, temperature, and geopotential height from the AIRS version 5, level 3 daily gridded product (AIRX3STD) between September 2002 and July 2010. Temperature and humidity profiles are used as input to the Fu-Liou radiative transfer code [Fu and Liou, 1992] to calculate the radiative cooling rates that are used in determining the clear-sky convergence profile, as explained in section 3.2. Geopotential heights are used to convert colocated CloudSat retrievals to a common pressure grid.

2.2. Microwave Limb Sounder

[11] We make use of temperature and water vapor mixing ratio measurements from the Microwave Limb Sounder (MLS) onboard the Aura satellite [Waters *et al.*, 2006]. MLS scans downward through the atmospheric limb to retrieve profiles by observing millimeter and submillimeter wavelength thermal emission in the instrument's field of view. Measurements are made simultaneously and continuously during both night and day, and are relatively insensitive to aerosol or thin high clouds.

[12] We use MLS version 2.2 (v2.2) Level 2 temperature and humidity data to supplement the AIRS profiles in the upper troposphere–lower stratosphere for the period August 2004 through July 2010. Both the temperature and water vapor data from MLS were screened for all flags described in the data quality and description document.

[13] Atmospheric temperature and pressure are retrieved based on emission from the spectral lines of molecular oxygen at 118 and 239 GHz. The vertical resolution is ~ 13 km at 0.001 hPa, increasing to 6 km at 316 hPa, and to 3 km at 31.6 hPa [Schwartz *et al.*, 2008]. Temperature precision is ~ 3 K at 0.001 hPa, increasing to 1 K or better from 3.16 hPa to 316 hPa [Schwartz *et al.*, 2008].

[14] The water vapor product is taken from the 190 GHz retrieval and has vertical resolution of 3.5 km between 4.5 hPa and 147 hPa increasing to 1.5 km at 316 hPa. Between 316 and 147 hPa, MLS v2.2 has an accuracy better than 25% for water vapor mixing ratios less than 500 ppmv [Read *et al.*, 2007]. The precision increases from 25% at 147 hPa to 65% at 316 hPa [Read *et al.*, 2007].

2.3. MODIS

[15] MODIS is a whiskbroom-scanning radiometer with 36 channels between 0.415 and 14.235 μm . The cloud detection algorithm provides a measure of the confidence that the field of view is clear [Platnick *et al.*, 2003]. Cloud top pressure (CTP) is inferred using CO_2 slicing within the 15 μm absorption band. The 0.65, 0.86, and 1.2 μm bands are used to retrieve optical thickness (τ), but these data are restricted to daytime observations.

[16] We make use of cloud fraction, CTP and τ from the Aqua MODIS 5 km level 2 Joint product over the period September 2002 to July 2010. After removing retrievals in which the cloud mask is undetermined or affected by sun glint, we calculate CTP- τ joint histograms of cloud fraction at 1° horizontal resolution, with 50 hPa-wide CTP bins

between 50 and 1000 hPa and the same τ bins of Kubar *et al.* [2007].

2.4. CloudSat

[17] The primary instrument on CloudSat is the 94 GHz nadir-pointing Cloud Profiling Radar (CPR) that measures the power backscattered from cloud particles as a function of distance from the radar [Stephens *et al.*, 2002]. We make use of the 2B-GEOPROF (Cloud Geometrical Profile) Release 4 Version 011 product between June 2006 and July 2010 and process it onto a 1° horizontal and 250 m vertical grid. The GEOPROF algorithm creates a cloud mask for those vertical levels in which the CPR receives a significant echo [Stephens *et al.*, 2002].

[18] We create a binary cloud mask containing ones where the GEOPROF cloud mask value is greater than or equal to 20. From this, we compute a binary profile of cloud tops by locating every bin with a value of one directly below a bin with a value of zero. Finally, to facilitate comparison with other data sets, we interpolate the CloudSat data from its native geometric height grid to a pressure grid using colocated AIRS retrievals of geopotential height and to a temperature grid using the combined AIRS-MLS temperatures described in section 3.1.

2.5. ISCCP

[19] We make use of the GCM simulator-oriented ISCCP cloud product (R. Pincus *et al.*, Reconciling simulated and observed views of clouds: MODIS, ISCCP, and the limits of instrument simulators, submitted to *Journal of Climate*, 2011) covering the period July 1983–June 2008. This product is derived from the ISCCP-D1 cloud data set [Rossow and Schiffer, 1999], which is a 3-hourly global data set on an equal-area grid, providing cloud fractions as joint functions of seven cloud top pressure bins and six optical depth bins. Scenes are classified as cloudy if the IR or VIS radiance in the 4–7 km field of view differs from the clear-sky value by more than the detection threshold. Optical thickness and cloud top temperature are computed for each cloudy scene by comparing the observed IR or VIS radiance with that computed from a radiative transfer model, and a temperature profile from the TIROS Operational Vertical Sounder is used to determine cloud top pressure.

[20] The ISCCP algorithm is generally unable to accurately determine the optical depth if it detects a cloud based on the IR threshold but the visible reflectance is very close to the expected clear-sky value [Marchand *et al.*, 2010]. In this situation, the ISCCP algorithm assigns the cloud top temperature to the expected tropopause temperature minus 5 K, with a resulting cloud top pressure near that of the tropopause. We have chosen to consider only clouds assigned to optical depth bins exceeding 1.3 in our analysis. Removing the thinnest cloud types results in a tropical mean ISCCP cloud top profile that is similar to that derived by the other instruments, with a peak in the 180–310 hPa bin (as discussed in section 4.1) (see also Pincus, submitted manuscript, 2011).

2.6. Clouds and the Earth's Radiant Energy System

[21] We make use of TOA total-sky LW and SW fluxes from several products derived from measurements made by the Clouds and the Earth's Radiant Energy System (CERES)

instruments onboard both Aqua and Terra spacecrafts [Wielicki *et al.*, 1996]. These fluxes are used in combination with ERA Interim data described in section 2.7 to compute monthly mean values of SW and LW cloud forcing. We have chosen to use several CERES products to assess the extent to which the derived signals are sensitive to the variety of assumptions made in deriving the products, the period of record, and the satellite platform from which the fluxes are measured.

[22] The CERES Edition 2.6 “lite” data sets use Edition 3 calibration and Edition 2 processing to remove all known CERES instrument artifacts. We use total-sky TOA fluxes from the SSF-lite Edition 2.6 and SYN-lite Edition 2.6 products, which are 1° gridded monthly mean data sets. The products derived from CERES on Aqua (Terra) cover the period July 2002 (March 2000) through December 2010. As described in the Edition 2.6 Data Quality Summary provided by the CERES Science Team, both SYN and SSF products are derived by temporally interpolating the TOA radiative fluxes between the CERES observation times to compute a complete 1-hourly data set for each month, which is then averaged to monthly means if a sufficient number of CERES measurements are available. Whereas the SYN product is derived using 3-hourly geostationary satellite data to estimate the diurnally varying flux in between CERES measurements, SSF assumes constant meteorology between CERES measurements and does not account for regional diurnal changes in flux and cloud properties. The SYN product is expected to be more reliable than the SSF product in regions with large diurnal cycles, but the opposite is the case in regions that have weak diurnal cycles or at large spatial scales because the SSF is free of any artifacts arising from the use of geostationary data in the algorithm.

[23] The Energy Balanced and Filled (EBAF) Edition 2.6 product, as described in the Edition 2.6 Data Quality Summary provided by the CERES Science Team, is derived from both the SYN and SSF products, but adjusts the LW and SW fluxes within their range of uncertainty to bring the globally averaged net TOA flux anomaly and global ocean-atmosphere heat storage into better agreement. Additionally, MODIS measurements are used to infer the clear-sky fluxes in regions where the CERES footprint is not classified as clear; thus all gaps in the clear-sky flux maps are filled. To improve the accuracy of diurnal corrections, observations from CERES on both Aqua and Terra satellites are used in the EBAF product starting in July 2002. The EBAF product covers the period March 2000 through December 2010.

2.7. ERA Interim Reanalysis

[24] We use monthly mean temperature, specific humidity, and surface albedo fields from the ERA Interim reanalysis [Dee *et al.*, 2011]. This data set is the latest global reanalysis product produced by the European Center for Medium-Range Weather Forecasts (ECMWF). We compute monthly anomalies from the monthly mean annual cycle over the period March 2000–February 2010. These anomalies are multiplied by clear-sky and all-sky radiative kernels [Soden *et al.*, 2008] to generate clear-sky radiative flux anomalies and cloud masking adjustments. The former will be used in place of CERES-derived clear-sky flux anomalies (which have gaps and are subject to clear-sky sampling biases) and the latter will be used to adjust the change in cloud forcing for noncloud-induced radiative flux anomalies. The clear-sky

fluxes and cloud masking adjustments derived from ERA Interim data are described in greater detail in section 4.4.

2.8. HadCRUT3v

[25] We make use of the globally gridded HadCRUT3v T_{sfc} data set, which is constructed using 4349 land stations along with marine data from in situ ship and buoy observations [Brohan *et al.*, 2006]. HadCRUT3v is the variance-adjusted version of the HadCRUT3 data set, meaning that each grid box’s anomalies are adjusted to account for a changing number of observing sites over the period of record.

3. Methodology

3.1. Combining AIRS and MLS Temperature and Humidity Profiles

[26] As shown by Kubar *et al.* [2007], the profile of clear-sky diabatic convergence and its fluctuations are sensitive to the structure of upper tropospheric–lower stratospheric (UTLS) temperature and humidity profiles. Unfortunately, the UTLS region is a particularly difficult area of the atmosphere to measure these quantities accurately [Kley *et al.*, 2000; Soden *et al.*, 2004]. In Figure 1 we show the area-weighted all-sky tropical mean temperature and humidity profiles in the UTLS region measured by AIRS and MLS, along with GPS occultation measurements of temperature from Constellation Observing System for Meteorology, Ionosphere, and Climate (COSMIC) [Anthes *et al.*, 2008]. (GPS mixing ratios are primarily model-generated in the UTLS, so they are not shown.) In general, the temperature profiles are in agreement at all levels, though AIRS places the cold-point tropopause somewhat lower in the atmosphere than do the other data sets. At pressures greater than about 150 hPa, AIRS and MLS mixing ratios are in good agreement as was shown by Read *et al.* [2007], but AIRS is significantly drier than MLS above this level.

[27] We have chosen to combine the AIRS and MLS temperature and humidity profiles in such a manner that each data set is used where it is most reliable, with a transition pressure of 200 hPa. The transition from AIRS to MLS data is done by giving increasing weight to the MLS data relative to the AIRS data as the 200 hPa level is approached from below.

3.2. Computation of Clear-Sky Radiative Cooling, Diabatic Subsidence, and Diabatic Convergence

[28] We follow the procedure described in section 3 of ZH10 to compute profiles of clear-sky radiative cooling (Q_R), diabatic subsidence (ω), and clear-sky diabatic convergence ($conv$). Briefly, we assume that clear-sky radiative cooling (calculated using the Fu-Liou radiation code, with zonal mean and monthly mean combined AIRS-MLS profiles of temperature and humidity as input) is exactly balanced by warming due to diabatic subsidence:

$$\omega = \frac{Q_R}{\sigma}. \quad (1)$$

σ is the static stability, which can be written

$$\sigma = \frac{\kappa T}{p} - \frac{\partial T}{\partial p}, \quad (2)$$

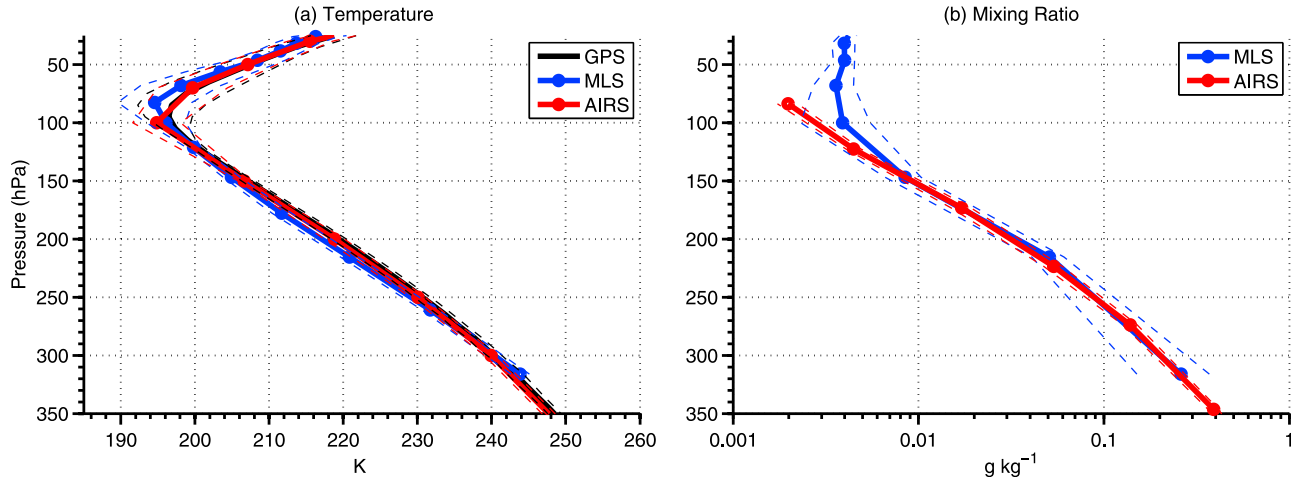


Figure 1. Tropical mean (a) temperature from COSMIC GPS occultation (black), MLS (blue), and AIRS (red) and (b) water vapor mixing ratio from MLS (blue) and AIRS (red). The dashed lines represent the 2σ range of monthly tropical average quantities. Note that mixing ratios are plotted on a log scale.

where $\kappa = R_d/c_p$, R_d is the gas constant for dry air, and c_p is the specific heat of air at constant pressure. Assuming mass continuity, the profile of $conv$ in the clear-sky region is calculated by

$$conv \equiv -\nabla_H \cdot \mathbf{U} = \frac{\partial \omega}{\partial p}. \quad (3)$$

Assuming a closed mass budget between convective and nonconvective regions, the rate of convergence into the clear-sky region is equivalent to the divergence out of the convective region. The peak in this radiatively driven mass divergence is a marker for the top of the rapidly mixed troposphere and is expected to be colocated with convectively detrained anvil clouds.

3.3. Regressions on Tropical Mean Surface Temperature Anomalies

[29] For each variable we first compute area-weighted tropical mean monthly means over their period of record. We then compute anomalies of each monthly mean data point from this average annual cycle of monthly data. Sensitivities to tropical mean surface temperature ($\overline{T_{sfc}}$) are calculated as regression coefficients between each variable and $\overline{T_{sfc}}$ anomalies. Estimates of the uncertainty in the derived regression slopes are computed using a bootstrapping method in which the residuals from the regression slope are resampled with replacement 10,000 times to compute a distribution of possible regression coefficients [Efron and Tibshirani, 1993]. The 2.5 and 97.5 percentiles of the regression slope distribution represent the 95% confidence interval surrounding each regression slope, and we consider slopes for which this confidence interval excludes zero to be statistically significant.

4. Results

4.1. Consistency Between High Cloud Fraction and Diabatic Convergence

[30] In Figure 2 we show the tropical mean combined AIRS-MLS mixing ratio and temperature profiles, Q_R cal-

culated with the Fu-Liou radiative transfer code, and σ , ω , and $conv$ calculated by equations (1–3). Tropical temperatures approximately follow the moist adiabat [Xu and Emanuel, 1989] at pressures greater than about 300 hPa, above which the temperature profile becomes increasingly more stable with height than the moist adiabat. Mixing ratios decrease exponentially with decreasing pressure due to the exponential dependence of saturation vapor pressure on temperature and the decrease in temperature with decreasing pressure. At pressures greater than 250 hPa, Q_R is roughly constant at about 1.5 K dy^{-1} . Above this level, Q_R decreases dramatically with decreasing pressure. Static stability, given by equation (2), is small and roughly constant with pressure up to about 250 hPa, above which point the increasing dominance of ozone heating over water vapor cooling causes the lapse rate to be increasingly more stable than the dry adiabat. The implied ω that is necessary to balance Q_R , given by equation (1), is relatively constant at 30 hPa dy^{-1} at pressures greater than 250 hPa, then decreases rapidly with decreasing pressure, reaching a value of zero at about 100 hPa (where Q_R is also zero). The rapid decrease of ω is related to both the rapid decrease of Q_R and the rapid increase of σ in the upper troposphere. The implied upper tropospheric $conv$, given by equation (3), exhibits a large peak at 200 hPa where the decrease of ω with decreasing pressure is most dramatic.

[31] Profiles of tropical mean cloud top frequency of occurrence from CloudSat as well as cloud top fraction from AIRS, MODIS, and ISCCP are shown in Figure 3. Recall that in the case of ISCCP, only clouds with optical depths exceeding 1.3 are included because the ISCCP retrieval algorithm places a questionably large fraction of clouds into the highest, thinnest bin of the histogram. Overlain as red lines for comparison is the $conv$ profile shown in Figure 2.

[32] It is important to bear in mind that $conv$ is a measure of the *net* convergence into the clear-sky regions that is required by the net diabatic tropical overturning. Thus one should not interpret $conv$ as a quantity to which cloud fraction should be proportional at every height. (If this were the case, cloud fraction would be zero or even negative

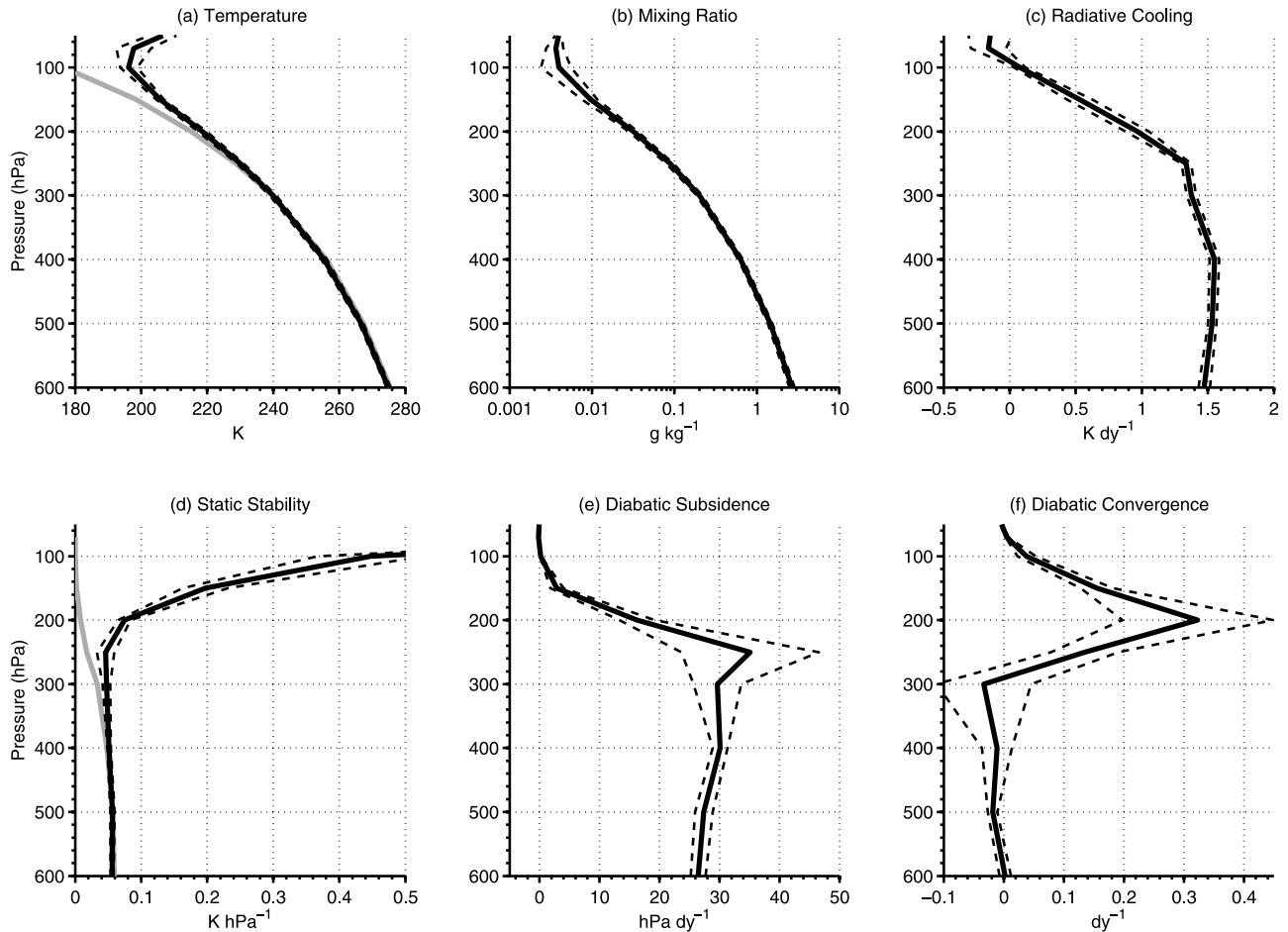


Figure 2. Tropical mean (a) temperature, (b) water vapor mixing ratio, (c) radiative cooling, (d) static stability, (e) diabatic subsidence, and (f) diabatic convergence. Temperature and mixing ratio retrievals are from the combination of AIRS and MLS, radiative cooling is calculated with the Fu-Liou radiative transfer code, and the other terms are calculated according to equations (1)–(3). Overlain in gray are the temperature (Figure 2a) and static stability (Figure 2d) for a moist adiabat with an 850 hPa temperature equal to that observed. The dashed lines represent the 2σ range of monthly tropical average quantities. Note that mixing ratios are plotted on a log scale.

throughout most of the lower and middle troposphere.) Rather, the integrated *conv* is a measure of the net mass flux in the divergent circulation of the tropics, the upper tropospheric branch of which is associated with detrainment from deep convection and its attendant anvil cloud coverage.

[33] The peak in the profile of *conv* is remarkably well correlated with the peak in the cloud profiles from all data sets, though in general, the peaks in AIRS and MODIS cloud top fraction and CloudSat cloud top frequency of occurrence tend to lie slightly above the peak in *conv*. Clearly the peak in the profile of *conv* serves as a convenient marker for the emission level of the bulk of tropical high clouds.

4.2. Tropical Mean T_{sfc} Fluctuations and Their Associated Cloud Anomalies

[34] We are interested in the sensitivity of cloud fields to T_{sfc} and how well this sensitivity is diagnosed by the anomalies in *conv*. Since we will focus primarily on the data-rich period of the A-Train, Figure 4 shows the time series of T_{sfc} anomalies from the HadCRUT3v data set over the period September 2002–December 2010.

[35] The dominant feature is a notable transition from the fairly neutral conditions that prevailed until early 2007 to a strong La Niña by the beginning of 2008, followed by a steady warming to a strong El Niño by the beginning of 2010 and a subsequent return to neutral conditions by mid-2010. Surface temperature anomalies associated with a tropical mean warming (not shown) exhibit a typical central Pacific El Niño pattern [Kao and Yu, 2009], with massive warm anomalies in the central tropical Pacific straddled by cold anomalies to the north, south, and west, and large cold anomalies in southeastern North America and midlatitude Eurasia.

[36] Before proceeding, we assess the robustness of the temperature and moisture fluctuations in the upper troposphere by comparing the COSMIC, MLS, and AIRS data sets (Figure 5). All three data sets exhibit a pronounced warming that extends up to about 200 hPa of between 2 and 2.5 K per degree of tropical mean surface warming. All three data sets also exhibit large negative temperature anomalies in the lower stratosphere that peak around -2 K K^{-1} between 50 and 65 hPa. Whereas AIRS temperature

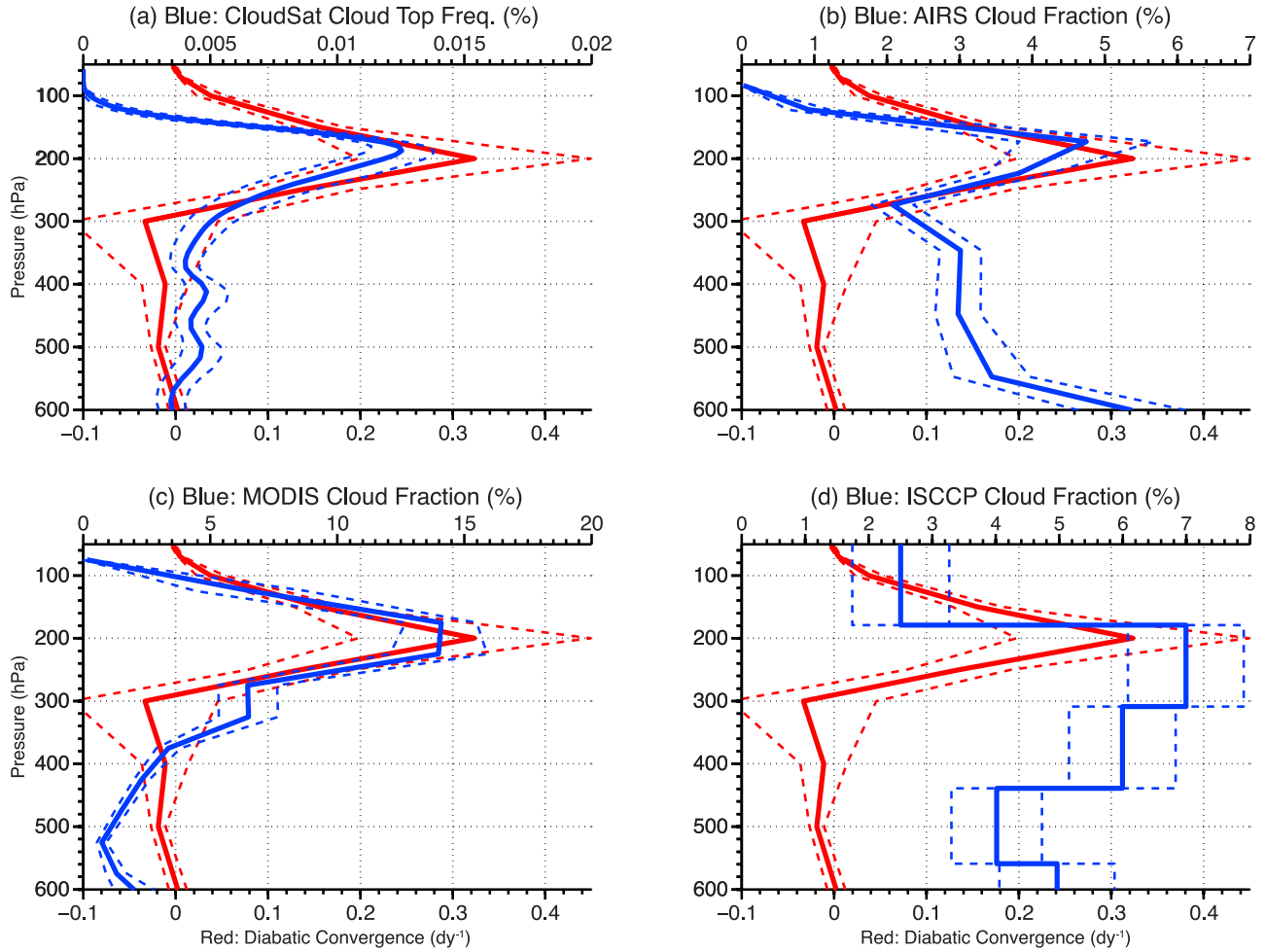


Figure 3. Tropical mean (a) cloud top frequency of occurrence from CloudSat and cloud fraction from (b) AIRS, (c) MODIS, and (d) ISCCP (blue). MODIS cloud fractions are plotted at the geometric mean pressure of the cloud top pressure bins. Only clouds with $\tau \geq 1.3$ are included in the ISCCP cloud fraction plot. Overlain red lines show the diabatic convergence repeated from Figure 2f. The dashed lines represent the 2σ range of monthly tropical average quantities. Note that the range of values on the upper x axis varies.

anomalies exhibit a sharp linear decrease above 200 hPa, MLS and GPS anomalies transition more smoothly to a maximum negative value at about 65 hPa. Since MLS and GPS have better vertical resolution in the upper troposphere and lower stratosphere, and agree well with each other, they may be more correct. The exact slope of the falloff of temperature anomalies with decreasing pressure affects the σ anomalies in the UTLS region, which impacts the implied diabatic subsidence and convergence anomalies. Thus our assessment of convergence changes as well as our determination of cloud top temperature changes are quite sensitive to the data set chosen.

[37] AIRS-observed and MLS-observed water vapor mixing ratio sensitivities are not statistically different from each other, which is reassuring considering that humidity fluctuations affect Q_R anomalies and therefore the implied subsidence and convergence. AIRS mixing ratio anomalies exhibit a less-rapid falloff with decreasing pressure above 175 hPa compared with MLS measurements. Near 200 hPa,

where our combined product is weighted equally by both products, MLS-measured mixing ratios exhibit greater sensitivity to tropical mean temperature fluctuations than do those measured by AIRS. This may be a result of sampling biases: AIRS humidity profiles cannot be successfully retrieved in overcast scenes whereas MLS measurements are less sensitive to clouds and can sample a wider range of humidities. Still, considering the myriad difficulties in measuring water vapor in the UTLS, the level of agreement in the anomalies is noteworthy.

[38] The vertical structure of temperature and humidity fluctuations has implications for the profile of $conv$. In Figure 6 we show the sensitivity of tropical mean temperature, water vapor mixing ratio, Q_R , σ , ω , and $conv$ to \bar{T}_{sfc} . The entire troposphere up to just above 100 hPa warms in association with tropical mean warming, with a peak warming occurring at about 200 hPa. Water vapor mixing ratios increase at all pressure levels, but most dramatically between 100 and 300 hPa. Q_R anomalies mimic the

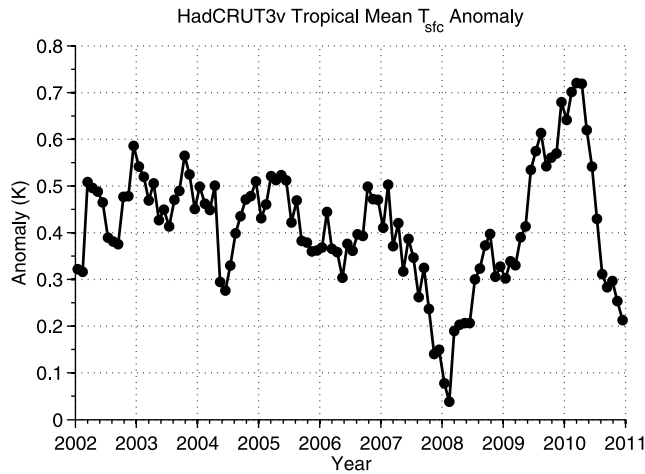


Figure 4. HadCRUT3v tropical mean surface air temperature anomalies relative to the 1961–1990 mean. Sea surface temperatures are used in place of surface air temperatures over the ocean.

humidity anomalies such that where water vapor concentrations increase, Q_R also increases, as expected from the FAT hypothesis. σ increases slightly up to about 250 hPa, then decreases substantially at pressures below 250 hPa. This structure is primarily governed by the vertical structure of warming, which peaks at 200 hPa and fairly rapidly transitions to cooling above 100 hPa.

[39] At pressures less than 250 hPa, the combination of enhanced Q_R and reduced σ results in an increase in ω . Conversely, at pressures greater than 250 hPa, the combination of enhanced σ overcompensating for enhanced Q_R results in a decrease in ω . Increased (reduced) ω above (below) the level of peak *conv* represents a reduction in the vertical derivative of ω , which reduces the *conv* peak. Peak enhancement of ω occurs at 200 hPa, resulting in anomalous *conv* above 200 hPa. Thus the net effect of a 1 K increase in

$\overline{T_{sfc}}$ is that the convergence profile shifts upward and exhibits a smaller peak value, much as it does in GCMs under greenhouse warming (ZH10).

[40] Sensitivity of observed cloud top profiles to a 1 K increase in $\overline{T_{sfc}}$ are shown in Figure 7, along with the sensitivity of the *conv* profile to warming repeated from Figure 6f. All data sets exhibit large reductions in cloud top fraction or frequency around 200–250 hPa (i.e., near the peaks in their respective mean profiles). Furthermore, cloud fractions from all data sets exhibit increases at pressures less than about 200 hPa (though positive MODIS cloud top fraction anomalies are not statistically significant). The structure of these cloud changes is well diagnosed by the change in *conv* profile.

[41] The profile of anomalous cloud tops from CloudSat shows a remarkable similarity to the profile of anomalous upper tropospheric *conv*, with both having the same location of zero crossing. At pressures less than (greater than) 150 hPa, both convergence and cloud top frequency increase (decrease). The greatest reductions in cloud top occurrence occur at the pressure of peak mean cloud top occurrence. That anomalous cloud tops measured by CloudSat most closely track the anomalous convergence profile is very reassuring given CloudSat's superior vertical resolution relative to that of the other sensors.

[42] The upward shift and reduced peak in the convergence and cloud profiles observed here are similar to those that accompany a warming climate in GCMs (ZH10), but we demonstrate in section 4.3 that the shift in cloud profile is accompanied by smaller changes in cloud top temperature (i.e., the response is more isothermal than in models).

[43] What is perhaps most striking is that the cloud profiles from all data sets exhibit a decrease in cloud coverage at and below their peak level that exceed increases in cloud coverage aloft. This is consistent with the net decrease in clear-sky convergence (i.e., the large decrease in *conv* at pressures greater than 150 hPa exceeds the increase at pressures less than 150 hPa). Although these net high cloud

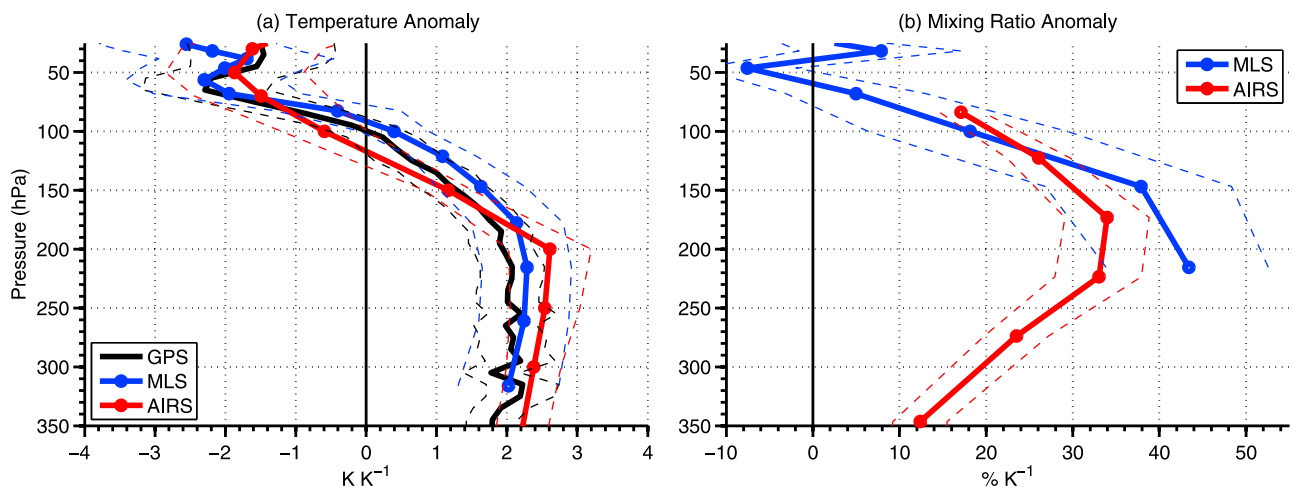


Figure 5. Sensitivity of (a) tropical mean temperature from COSMIC GPS occultation (black), MLS (blue), and AIRS (red) and (b) water vapor mixing ratio from MLS (blue) and AIRS (red). Sensitivity profiles are computed by regressing the anomaly at each pressure by the tropical mean surface temperature anomaly. The dashed lines represent the 95% confidence intervals of the regression coefficients computed using a bootstrapping method as described in the text.

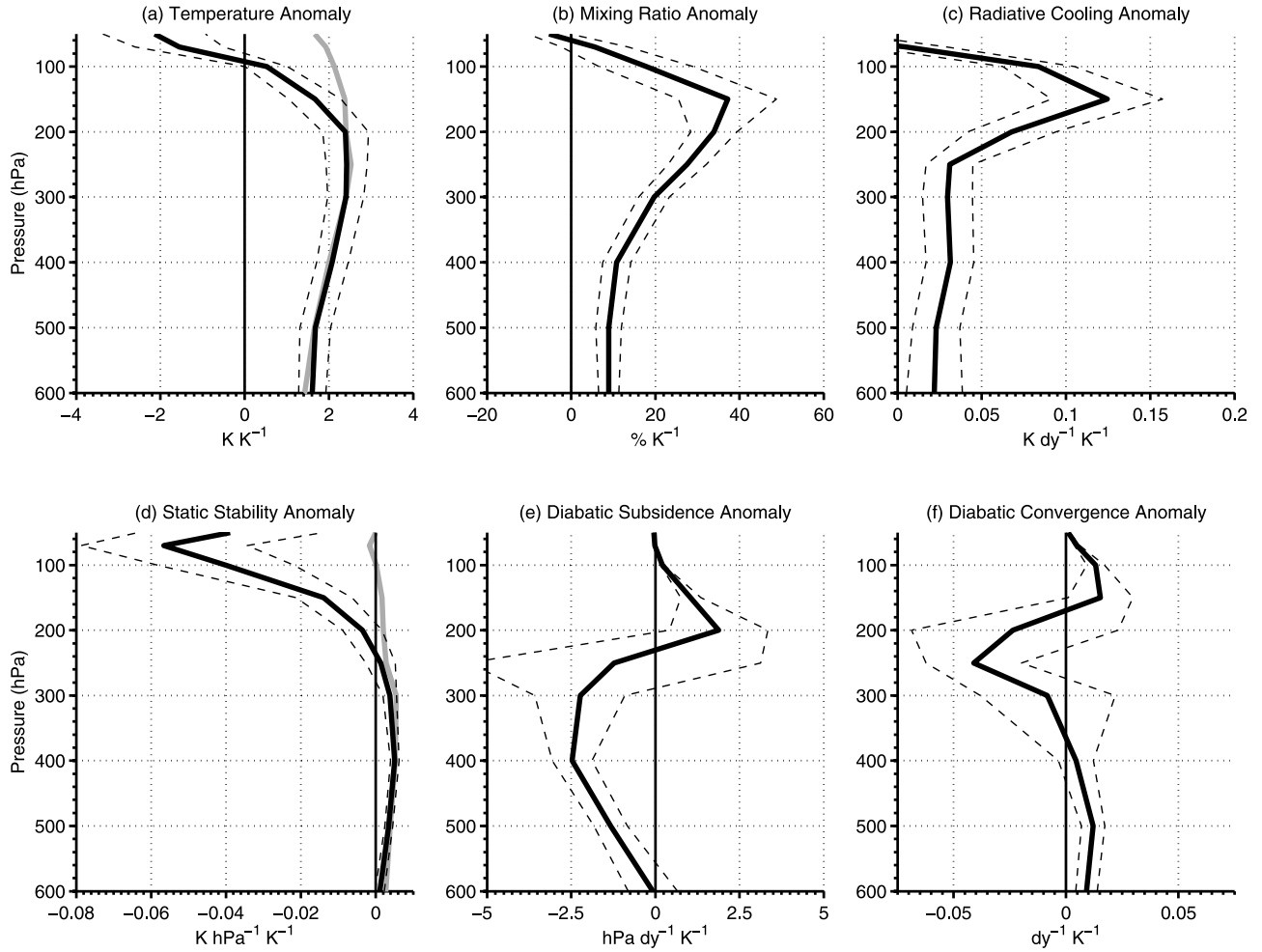


Figure 6. Sensitivity of (a) tropical mean temperature, (b) water vapor mixing ratio, (c) radiative cooling, (d) static stability, (e) diabatic subsidence, and (f) diabatic convergence to tropical mean surface temperature. Sensitivity profiles are computed by regressing the anomaly at each pressure by the tropical mean surface temperature anomaly. The dashed lines represent the 95% confidence intervals of the regression coefficients computed using a bootstrapping method as described in the text. Overlain in gray is the sensitivity of the temperature (Figure 6a) and static stability profiles (Figure 6d) of the moist adiabat shown in Figure 2 to a 1 K increase in surface temperature.

and *conv* reductions are not statistically significant, they lend support to an irislike response in high cloud coverage that is directly related to the decrease in upper tropospheric clear-sky convergence as the tropics warms. Note that the mechanism invoked for such cloud changes is quite different from that of *Lindzen et al.* [2001] in that it has nothing to do with cloud microphysics, but relies only on mass and energy budget considerations that show apparent skill in predicting high cloud changes.

4.3. FAT or PHAT?

[44] An important finding in the work of ZH10 is that GCM cloud fraction profiles shift upward, but less so than do the isotherms. This meant that the cloud-weighted temperatures increased very slightly rather than staying constant as expected from the FAT hypothesis. This nonisothermal shift in cloud profile was well diagnosed by the shift in upper tropospheric convergence and was caused by increases in σ at all temperatures.

[45] In Figure 8 we plot the variables shown in Figure 2, but as functions of temperature. Water vapor concentrations are fundamentally limited by temperature via the Clausius-Clapeyron relation; thus the profile of mixing ratio remains nearly constant in temperature coordinates. Because Q_R is primarily due to water vapor rotation lines in the upper troposphere, its profile is also largely unchanged when plotted as a function of temperature, though cooling is slightly enhanced at temperatures colder than 210 K where moisture increases and the lapse rate increases with tropical warming.

[46] Unlike the case of GCM-simulated global warming in which σ increased significantly at every temperature (compare Figure 4c of ZH10), here σ increases only very slightly when plotted as a function of temperature. At most temperatures, the perturbation profile is not statistically different from the mean profile. The slight increase in σ at all but the coldest temperatures causes a small reduction in ω , which results in a smaller *conv* peak that is shifted to

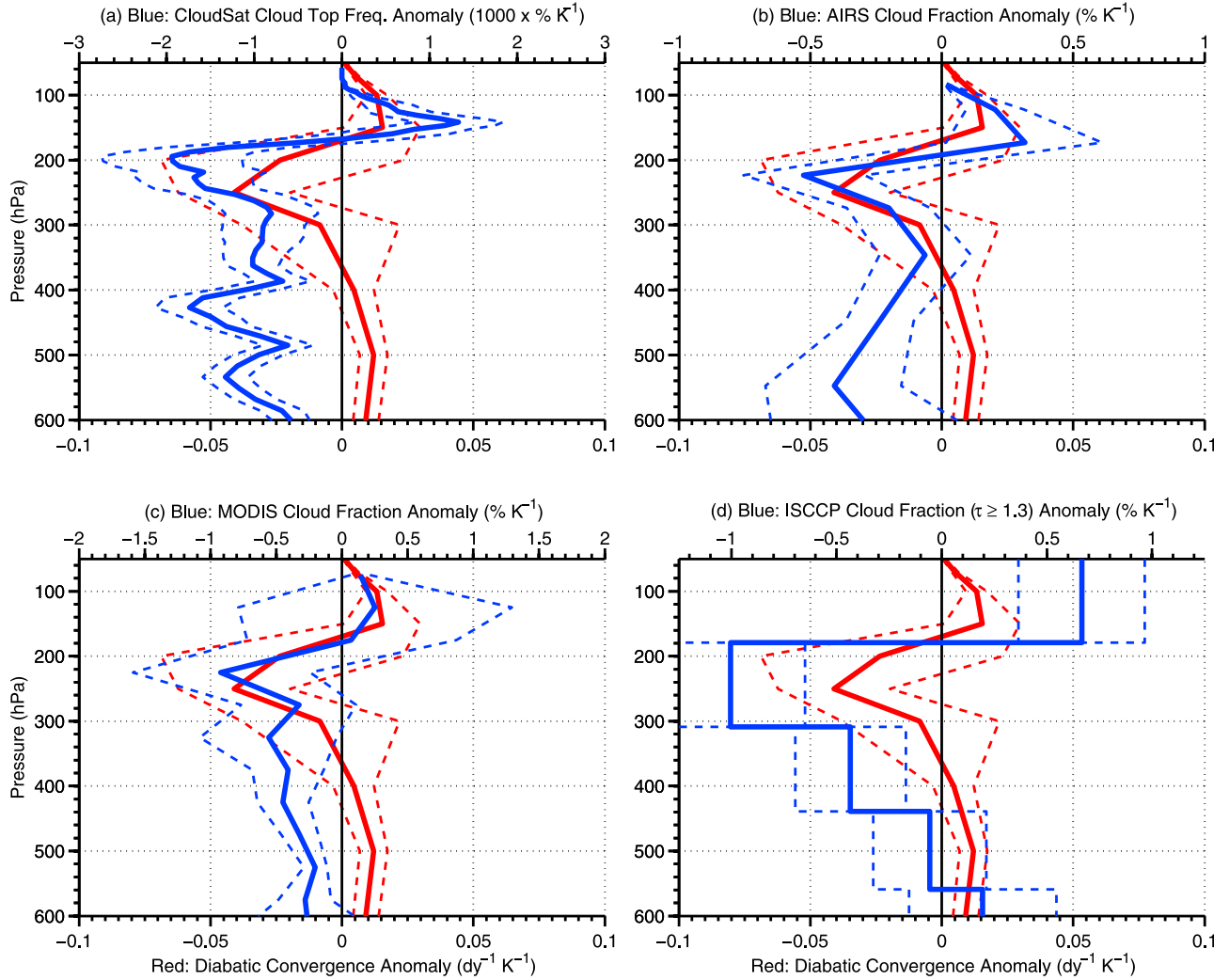


Figure 7. Sensitivity of (a) tropical mean cloud top frequency of occurrence from CloudSat and cloud fraction from (b) AIRS, (c) MODIS, and (d) ISCCP to tropical mean surface temperature (blue). Only clouds with $\tau \geq 1.3$ are included in the ISCCP cloud fraction plot. Overlain in red is the sensitivity of diabatic convergence to tropical mean surface temperature as shown in Figure 6f. Note that the range of values on the upper x axis varies. The dashed lines represent the 95% confidence interval of the regression coefficients computed using a bootstrapping method as described in the text.

warmer temperatures. The perturbed *conv* profile is statistically indistinguishable from its mean profile, indicating that it shifts upward (Figure 6f) in such a way as to remain at nearly the same temperature (Figure 8f), consistent with the expectations from the FAT hypothesis.

[47] The degree to which *conv* shifts upward isothermally depends on the σ response, so why do tropical σ responses to modeled global warming and to observed variability differ? Although modeled and observed σ responses are in close agreement at pressures for which temperature is moist adiabatic, they disagree at lower pressures where the lapse rate is subadiabatic (not shown). Specifically, GCM-simulated warming extends to higher altitudes and the transition from positive to negative σ anomalies occurs higher than in observations, possibly indicating differences in the response of ozone: in the GCMs analyzed by ZH10, ozone profiles are prescribed seasonally varying functions of pressure that either stay constant or slowly recover to preindustrial

levels over the course of the 21st century [Miller *et al.*, 2006], but in nature one would expect ozone (and its radiative heating) to decrease at pressure levels that become incorporated into the well-mixed troposphere, as discussed by Harrop and Hartmann (submitted manuscript, 2011). Indeed, cloud resolving model experiments of Kuang and Hartmann [2007] showed that cloud top temperatures remained fixed (increased) if ozone profiles are shifted upward (downward), demonstrating sensitivity to the location of ozone radiative heating in the upper troposphere.

[48] Because CloudSat provides the most highly resolved cloud top information, we compare its anomalies with those of the convergence profile as functions of temperature in Figure 9. The two profiles are remarkably similar, with decreased *conv* and cloud top coverage at all temperatures, but most dramatically between 200 and 220 K. A slight shift of both the peak in *conv* and the peak cloud amount toward warmer temperatures is apparent, though they are not

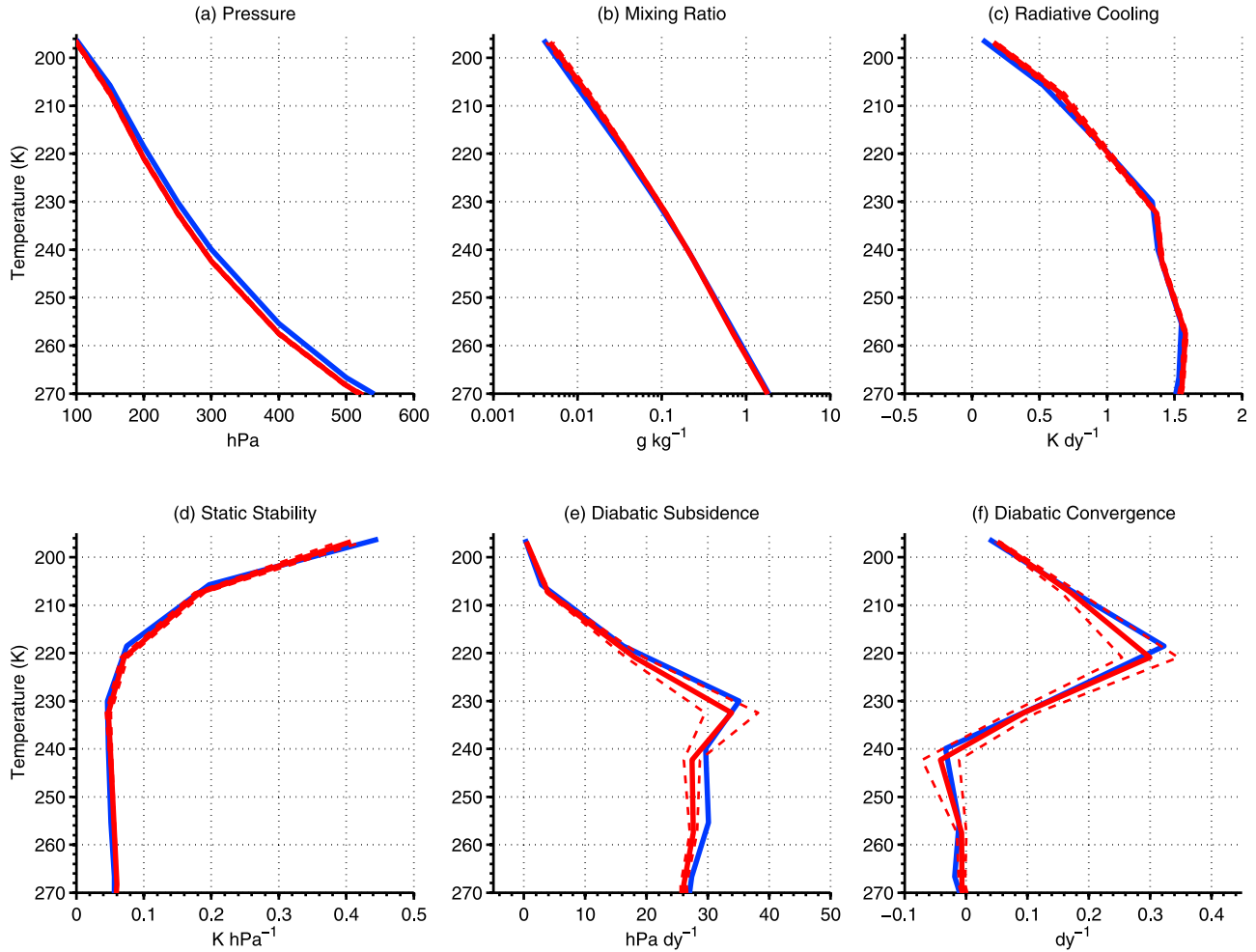


Figure 8. Tropical mean (a) pressure, (b) water vapor mixing ratio, (c) radiative cooling, (d) static stability, (e) diabatic subsidence, and (f) diabatic convergence (blue), along with the sum of the mean profiles and the perturbation profiles (red) shown in Figure 6, all plotted as functions of tropical mean temperature from AIRS-MLS. Dashed red lines represent the 95% confidence intervals of the perturbation profile.

statistically significant. Thus, we cannot rule out a purely isothermal (FAT-like) response of the cloud tops to tropical mean warming, but the results are suggestive of a proportionately higher temperature (PHAT-like) response, as seen in GCM simulations (ZH10). Differences in the vertical structure of warming between month-to-month fluctuations shown here and greenhouse warming in GCMs leads to subtle differences in cloud responses, but the basic constraint imposed by the clear-sky energy budget fairly accurately explains cloud changes in either case.

4.4. Radiative Impact of Observed Cloud Anomalies

[49] In this section we assess the implications of the observed cloud fluctuations for TOA radiation in two ways. First, we use histograms of MODIS-derived cloud fraction as a joint function of optical depth and cloud top pressure, combined with cloud radiative kernels generated using a radiative transfer model to calculate the impact of the observed cloud fraction changes on TOA radiative fluxes. Other than the following differences, the procedure for computing cloud radiative kernels is the same as in the

works of *Hartmann et al.* [2001b], *Kubar et al.* [2007], and M. D. Zelinka et al. (Computing and partitioning cloud feedbacks using cloud property histograms, Part I: Cloud radiative kernels, submitted to *Journal of Climate*, 2011) to which the reader is referred for the details of the procedure. We insert monthly mean AIRS temperature and humidity profiles into the Fu-Liou radiation code, along with synthetic profiles of liquid or ice water content that correspond to the cloud top pressure and optical depth at the midpoint of each MODIS histogram bin. TOA fluxes computed with and without synthetic clouds are differenced to compute the individual impact of each cloud type, resulting in a cloud radiative kernel. We compute LW and SW kernels (not shown) for each latitude equatorward of 30°, which are then multiplied by the anomalous cloud fraction histogram and summed over all bins to compute the effect of cloud fraction anomalies on TOA fluxes. Note that this gives an estimate of the radiative flux changes caused by clouds alone, with all other quantities held fixed. Thus, it is a direct estimate of cloud feedback, but we emphasize that

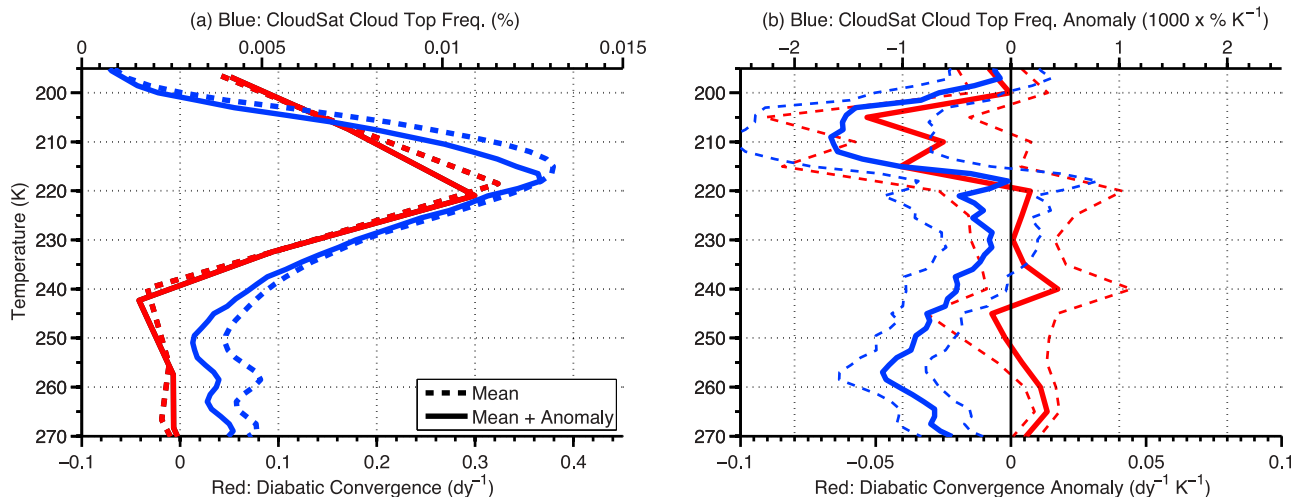


Figure 9. (a) Tropical mean CloudSat cloud top frequency of occurrence (blue) and diabatic convergence (red). The dashed lines represent the mean profile, and the solid lines represent the sum of the mean and perturbation profile shown in Figure 9b. (b) Sensitivity of tropical mean CloudSat cloud top frequency of occurrence (blue) and diabatic convergence (red) to tropical mean surface temperature. The dashed lines represent the 95% confidence intervals of the regression coefficients computed using a bootstrapping method as described in the text.

it is the cloud feedback in response to ENSO and not to CO_2 -induced global warming.

[50] In Figures 10a, 10b, and 10c we show the tropical mean MODIS cloud fraction histogram, the anomalous cloud fraction histogram corresponding to a 1 K perturbation in tropical mean surface temperature, and their difference. It is important to bear in mind that MODIS cloud fraction anomalies in many pressure and optical depth bins are statistically insignificant and that the cloud types included in the MODIS histogram do not represent all cloud types present. For example, *Marchand et al.* [2010]; Pincus et al., submitted manuscript, 2011 show that MODIS frequently does not retrieve optical depths for low broken clouds and optically thin ($\tau < 1$) high clouds; thus they will tend to be excluded from the MODIS histogram).

[51] Anvil (CTP < 450 hPa and $1 \leq \tau < 16$) and thick (CTP < 450 hPa and $\tau \geq 16$) clouds clearly rise in association with tropical warming, exhibiting reductions at pressures greater than about 180 hPa and smaller increases at pressures less than about 180 hPa. Largest fluctuations are evident in the anvil cloud fractions, which is consistent with the interpretation of *conv*, which one would expect to be physically related to mass detrainment and therefore anvil coverage. High thin clouds (CTP < 450 hPa and $\tau < 1$) exhibit reductions at all pressures. Additionally, low cloud fractions exhibit a broadening of their distribution in the vertical, as evidenced by decreases near their peak straddled above and below by large increases, but we note that MODIS may have difficulty determining the correct cloud top pressure for low clouds in regions of large temperature inversions, as reviewed by *Marchand et al.* [2010]. Neither AIRS nor CloudSat exhibit the negative cloud fraction anomalies seen by MODIS between about 725 and 850 hPa, but ISCCP cloud fraction anomalies are negative everywhere below 680 hPa (not shown). In Figures 10d, 10e, and 10f we show the product of the anomalous cloud fraction histogram with LW, SW, and net cloud radiative kernels.

The large decrease in anvil and thick clouds at and below the level of their respective peaks and slightly smaller increase above the level of their respective peaks is apparent in both the anomalous LW and SW cloud feedback diagrams. High cloud fractional changes are the dominant cause of changes in LW fluxes, whereas SW fluxes are sensitive to both high and low cloud changes. Despite an increase in cloud fraction at the lowest pressure bins, overall high cloud fraction (CTP < 450 hPa) decreases by about 1% in association with a 1 K tropical T_{sfc} anomaly, resulting in a negative LW high cloud feedback of $-1.0 \pm 1.3 \text{ W m}^{-2} \text{ K}^{-1}$. Conversely, the broad reductions in high cloud amount result in large decreases in reflection and therefore an implied positive SW high cloud feedback of $1.3 \pm 1.3 \text{ W m}^{-2} \text{ K}^{-1}$. The impact of high cloud changes on SW fluxes is opposed by that of low cloud changes, but nevertheless, the SW cloud feedback is positive in association with tropical warming (regression slope of $0.7 \pm 2.6 \text{ W m}^{-2} \text{ K}^{-1}$). In the net, high cloud feedback is positive, not primarily because of the enhanced greenhouse effect from rising cloud tops but rather because of the enhanced downwelling SW radiation from reduced high cloud coverage. However, the sign is not statistically significant, and a small negative feedback from high clouds cannot be ruled out.

[52] As an independent check of the sensitivities computed above, our second method uses more direct measures of cloud-induced radiative fluxes. We compute anomalies in tropical mean cloud radiative forcing using a combination of all-sky flux measurements from CERES and clear-sky flux estimates derived by applying the radiative kernels of *Soden et al.* [2008] to ERA Interim data. Clear-sky flux anomalies are computed by multiplying the monthly ERA Interim temperature, water vapor, and surface albedo anomalies with the appropriate clear-sky radiative kernels. We have chosen to use kernel-derived clear-sky fluxes rather than those retrieved by CERES for several reasons. First, the latter include sampling biases that can strongly impact cloud

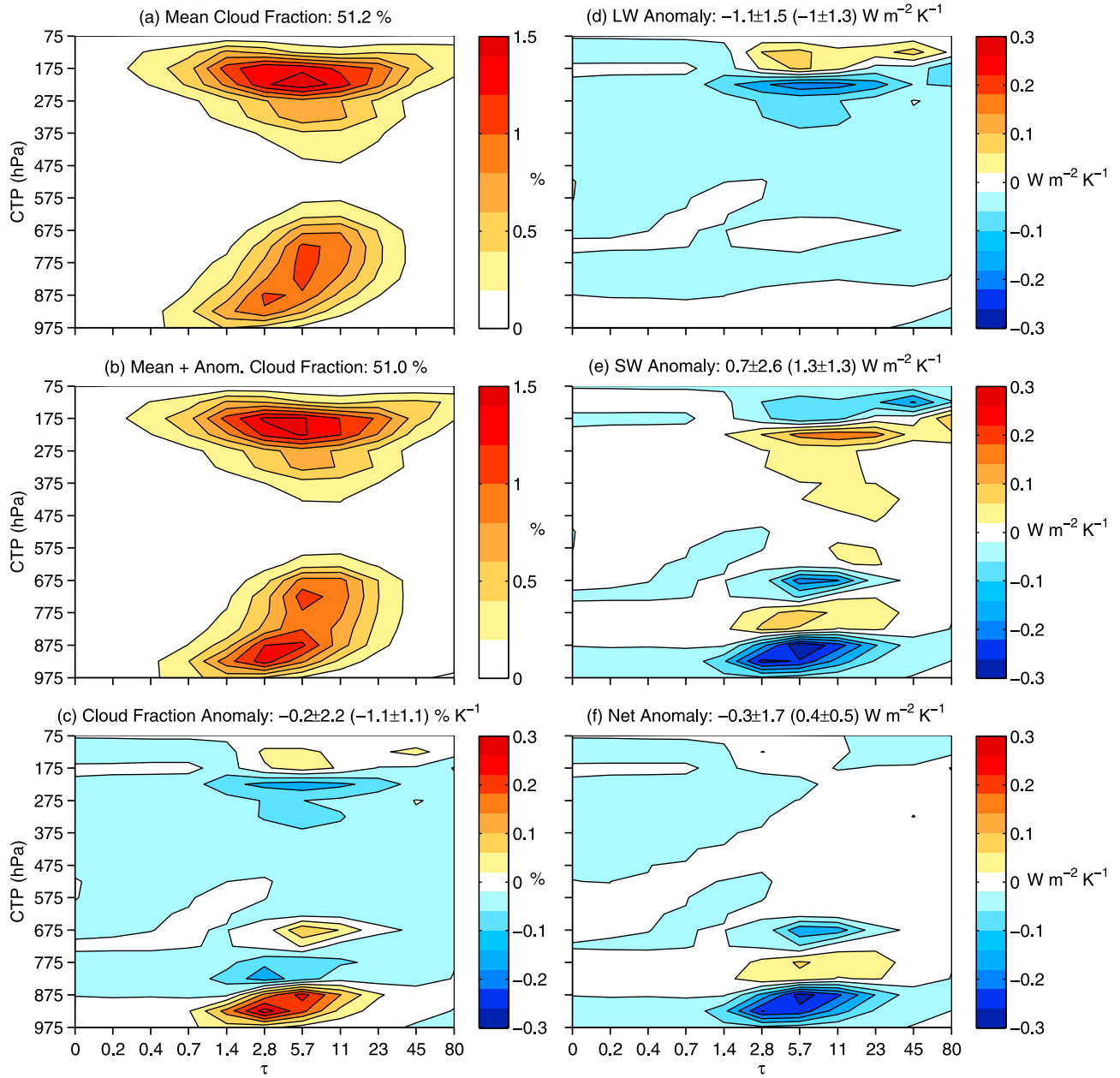


Figure 10. (a) Tropical mean MODIS cloud fraction as a joint function of cloud top pressure and optical depth, (b) the anomalous cloud fraction corresponding to a 1 K perturbation in tropical mean surface temperature, and (c) the sensitivity of tropical mean cloud fraction to a 1 K perturbation in tropical mean surface temperature. Also shown is the product of the cloud fraction sensitivity shown in Figure 10c with (d) LW, (e) SW, and (f) net cloud radiative kernels. The sensitivities of each quantity to tropical mean surface temperature computed by summing the histograms are shown in the titles. The contributions of high (CTP < 450) cloud anomalies are given in parentheses.

forcing estimates [Sohn and Bennartz, 2008]. Second, clear-sky retrievals are frequently unsuccessful in regions of persistent cloudiness where cloud forcing is large. Finally, clear-sky fluxes computed with radiative transfer models using observed temperature and humidity profiles have been shown to be accurate [Dessler *et al.*, 2008] and are not subject to sampling biases that arise from the constraint to retrieve in rare clear-sky scenes. By adjusting the cloud forcing anomalies for noncloud-induced effects following the method of Shell *et al.* [2008] and Soden *et al.* [2008], we

isolate the cloud-induced changes in TOA radiative fluxes, which is the appropriate quantity to compare with the cloud kernel-derived estimates. Following Dessler [2010], we regress these radiative flux anomalies on \overline{T}_{sfc} to get estimates of tropical cloud feedback. Estimates of LW, SW, and net cloud feedback from five CERES data sets are provided in Table 1, along with the values derived using the MODIS and ISCCP cloud fraction histograms.

[53] Every data set exhibits a negative LW cloud feedback and a positive SW cloud feedback in response to tropical

Table 1. Cloud Feedback Estimates in $\text{W m}^{-2} \text{K}^{-2}$ From Direct Measurements From Several CERES Data Sets and From Multiplying the Cloud Radiative Kernels by the Anomalous MODIS and ISCCP Cloud Fractions^a

Data Set	Temporal Coverage	LW	SW	Net
<i>Direct Measurements</i>				
Terra SSF	Mar 2000 to Dec 2010	-0.4 ± 1.0	0.8 ± 1.1	0.4 ± 1.3
Aqua SSF	Jul 2002 to Dec 2010	-0.8 ± 1.1	1.3 ± 1.2	0.4 ± 1.4
Terra SYN	Mar 2000 to Dec 2010	-0.7 ± 1.0	1.1 ± 1.1	0.4 ± 1.2
Aqua SYN	Jul 2002 to Dec 2010	-0.5 ± 1.2	0.6 ± 1.3	0.1 ± 1.4
Aqua + Terra EBAF	Mar 2000 to Dec 2010	-0.7 ± 1.0	0.7 ± 1.0	0.0 ± 1.2
<i>Cloud Radiative Kernel Estimates</i>				
Aqua MODIS	Sep 2002 to Jul 2010	-1.1 ± 1.5	0.7 ± 2.6	-0.3 ± 1.7
Aqua MODIS (high)	Sep 2002 to Jul 2010	-1.0 ± 1.3	1.3 ± 1.3	0.4 ± 0.5
ISCCP	Jul 1983 to Jun 2008	-0.3 ± 0.4	0.7 ± 1.3	0.4 ± 1.2
ISCCP (high)	Jul 1983 to Jun 2008	-0.2 ± 0.4	0.5 ± 0.4	0.3 ± 0.3

^aCERES data are supplemented with clear-sky fluxes and cloud masking adjustments from radiative kernels applied to ERA Interim data, as described in the text. Also provided are the 95% confidence intervals computed using a bootstrapping method as described in the text. Feedbacks for which the range of uncertainty excludes zero are in bold.

warming, though in most cases the error bars are large enough that the sign is uncertain. Exceptions to this are the significantly positive SW cloud feedbacks from the Aqua SSF and Terra SYN data sets and from high clouds in the MODIS and ISCCP data sets. All estimates fall within the error bars of each other. In all but the estimate derived using the full MODIS histogram, positive SWCF anomalies dominate over negative LWCF anomalies, suggesting that the net tropical cloud feedback in response to interannual variability is most likely positive.

[54] Our results are in qualitative agreement with those of Zhang *et al.* [1996], who find that both tropical mean LWCF and SWCF decrease in magnitude with warming, and also with Chung *et al.* [2010], who find that the reduction in OLR is overwhelmed by a reduction in reflected shortwave radiation. Su and Jiang (Tropical clouds and circulation changes during recent El Niños, submitted to *Geophysical Review Letters*, 2011) show that the net feedback operating on interannual time scales can be positive or negative depending on the pattern of warming, consistent with the fact that our error bars include feedbacks of both sign. Finally, our results for high clouds are in agreement with Lin *et al.* [2002], who showed using the same model as Lindzen *et al.* [2001] but with CERES fluxes that for a hypothetical “iris,” the SW effect would dominate over the LW effect.

5. Conclusions and Discussion

[55] We have demonstrated in this study that the upper tropospheric diabatic convergence (*conv*) that results from the balance of radiative cooling and subsidence warming in the clear-sky tropics provides a powerful tool for diagnosing both the vertical level and magnitude of peak tropical cloud coverage as measured by a suite of satelliteborne sensors. Furthermore, we have demonstrated that fluctuations in the profiles of tropical cloud coverage in association with interannual variability of surface temperature are well diagnosed by these clear-sky constraints. Specifically, as the tropics warms in association with ENSO, cloud fraction profiles exhibit an upward shift and reduction in peak coverage, a structure that is remarkably well diagnosed by *conv*.

[56] In agreement with the isothermal cloud response expected from the fixed anvil temperature hypothesis and

seen in the modeling studies of Hartmann and Larson [2002] and Kuang and Hartmann [2007] and observational studies of Xu *et al.* [2005, 2007] and Eitzen *et al.* [2009], the cloud profile exhibits small but insignificant variations when plotted in temperature coordinates. Small increases in static stability at all temperatures result in a statistically insignificant shift of the *conv* peak toward warmer temperatures, a pattern that is mimicked in the cloud profiles and is suggestive of the PHAT-like response seen in CMIP3 GCMs (ZH10).

[57] Finally, we have made use of CTP- τ joint histograms of cloud fraction from MODIS and ISCCP and cloud radiative kernels to estimate the effect of changing cloud distribution on TOA fluxes. The large decrease in anvil cloud coverage at and below its peak and the smaller increase above its peak in response to tropical warming result in a statistically insignificant net heating of the tropics primarily because the overall reduction in coverage enhances SW absorption more than it enhances LW emission. Feedback estimates derived using the full MODIS and ISCCP histograms lie within the uncertainties of estimates derived from CERES broadband fluxes, all of which exhibit a net positive tropical cloud feedback operating on interannual time scales. However, negative tropical net cloud feedbacks cannot be ruled out at the 95% confidence level, and we note that the sign of the feedback is likely sensitive to the pattern of SST anomalies (Su and Jiang, submitted manuscript, 2011).

[58] We wish to stress that the results of this study are not meant to suggest that radiation anomalies due to cloud changes associated with ENSO can be used as a surrogate for long-term cloud feedback due to CO₂-induced global warming, or that the long-term global mean SW cloud feedback is positive and LW cloud feedback is negative. Rather, we have shown that the clear-sky diabatic convergence is an effective metric for diagnosing the mean and change in amount, altitude, and temperature of peak high-level cloudiness in nature. These results, in combination with those of ZH10, lend credence to the utility of this tool for understanding high cloud changes due to climate fluctuations across time scales forced by a variety of mechanisms and for evaluating the realism of high cloud changes and their implied feedbacks in models.

[59] Dessler [2010] found no correlation between cloud feedbacks derived on short time scales and those derived on

long time scales. Our work offers a possible mechanism for explaining why cloud feedbacks (at least the component arising from tropical cloud changes) operating on different time scales are uncorrelated. Upper tropospheric amplification of warming is less vertically and horizontally extensive during El Niño than in global warming simulations [cf. Lu *et al.*, 2008, Figure 2]. This results in a smaller upward shift and a larger decrease in implied clear-sky upper tropospheric convergence accompanying El Niño than that accompanying global warming (not shown), and these features are mimicked in the cloud fields. Thus, the vertical structure of warming, through its impact on the clear-sky convergence profile, may determine the anomalous cloud structure that arises in response to a climate perturbation. Given that the vertical structure of warming differs considerably depending on the response of ozone and whether the warming is forced radiatively (e.g., by increasing CO₂) or by anomalous tropical air-sea heat fluxes (e.g., ENSO), it is inevitable that tropical clouds will exhibit a variety of responses to a given $\overline{T_{sfc}}$ anomaly. Thus, cloud feedbacks driven by short-term variability may have little relation to the long-term cloud feedback in response to increasing greenhouse gas concentrations.

[60] **Acknowledgments.** This research was supported by NASA grant NNX09AH73G, by NASA Earth and Space Science Fellowship NNX06AF69H, and by the Lawrence Livermore National Laboratory (LLNL) Institutional Postdoctoral Program. We thank Rob Wood for useful discussions and suggestions for improvement, Hui Su and two anonymous reviewers for detailed criticisms and comments on the paper, and Marc Michelsen for computer support. AIRS and MLS data used in this effort are archived and distributed by the Goddard Earth Sciences Data and Information Services Center. MODIS data are distributed by the Level 1 and Atmosphere Archive and Distribution System. CloudSat data are provided courtesy of the NASA CloudSat project. The GCM simulator-oriented ISCCP cloud product is provided courtesy of Y. Zhang at LLNL. CERES data were obtained from the NASA Langley Research Center EOSDIS Distributed Active Archive Center. ERA Interim data are provided by the European Centre for Medium-Range Weather Forecasts. HadCRUT3v data are provided by the Climatic Research Unit at the University of East Anglia, United Kingdom. This work was performed under the auspices of the U.S. Department of Energy by Lawrence Livermore National Laboratory under contract DE-AC52-07NA27344.

References

- Anthes, R. A., et al. (2008), The COSMIC/FORMOSAT-3 Mission: Early results, *Bull. Am. Meteorol. Soc.*, **89**, 313–333.
- Aumann, H. H., et al. (2003), AIRS/AMSU/HSB on the Aqua mission: Design, science objectives, data products, and processing systems, *IEEE Trans. Geosci. Remote Sens.*, **41**, 253–264.
- Bony, S., and J.-L. Dufresne (2005), Marine boundary layer clouds at the heart of tropical cloud feedback uncertainties in climate models, *Geophys. Res. Lett.*, **32**, L20806, doi:10.1029/2005GL023851.
- Bony, S., et al. (2006), How well do we understand and evaluate climate change feedback processes?, *J. Clim.*, **19**, 3445–3482.
- Brohan, P., J. J. Kennedy, I. Harris, S. F. B. Tett, and P. D. Jones (2006), Uncertainty estimates in regional and global observed temperature changes: A new data set from 1850, *J. Geophys. Res.*, **111**, D12106, doi:10.1029/2005JD006548.
- Chae, J. H., and S. C. Sherwood (2010), Insights into cloud-top height and dynamics from the seasonal cycle of cloud-top heights observed by MISR in the west Pacific region, *J. Atmos. Sci.*, **67**, 248–261.
- Chambers, L. H., B. Lin, B. Wielicki, Y. X. Hu, and K. M. Xu (2002), Reply to comments on “The Iris Hypothesis: A negative or positive cloud feedback?,” *J. Clim.*, **15**, 2716–2717.
- Chung, E.-S., B. J. Soden, and B.-J. Sohn (2010), Revisiting the determination of climate sensitivity from relationships between surface temperature and radiative fluxes, *Geophys. Res. Lett.*, **37**, L10703, doi:10.1029/2010GL043051.
- Dee, D. P., et al. (2011), The ERA-Interim reanalysis: Configuration and performance of the data assimilation system, *Q. J. R. Meteorol. Soc.*, **137**, 553–597, doi:10.1002/qj.828.
- Del Genio, A. D., and W. Kovari (2002), Climatic properties of tropical precipitating convection under varying environmental conditions, *J. Clim.*, **15**, 2597–2615.
- Dessler, A. E. (2010), A determination of the cloud feedback from climate variations over the past decade, *Science*, **330**, 1523–1527, doi:10.1126/science.1192546.
- Dessler, A. E., P. Yang, J. Lee, J. Solbrig, Z. Zhang, and K. Minschwaner (2008), An analysis of the dependence of clear-sky top-of-atmosphere outgoing longwave radiation on atmospheric temperature and water vapor, *J. Geophys. Res.*, **113**, D17102, doi:10.1029/2008JD010137.
- Efron, B., and R. J. Tibshirani (1993), *An Introduction to the Bootstrap*, *Monogr. Stat. Appl. Probab.*, vol. 57, edited by R. L. Smith et al., 436 pp., Chapman and Hall, Boca Raton, Fla.
- Eitzen, Z. A., K.-M. Xu, and T. Wong (2009), Cloud and radiative characteristics of tropical deep convective systems in extended cloud objects from CERES observations, *J. Clim.*, **22**, 5983–6000.
- Fu, Q., and K. N. Liou (1992), On the correlated k-distribution method for radiative transfer in nonhomogeneous atmospheres, *J. Atmos. Sci.*, **49**, 2139–2156.
- Harrison, H. (2002), Comments on “Does the Earth have an adaptive infrared iris?,” *Bull. Am. Meteorol. Soc.*, **83**, 597.
- Hartmann, D. L., and K. Larson (2002), An important constraint on tropical cloud-climate feedback, *Geophys. Res. Lett.*, **29**(20), 1951, doi:10.1029/2002GL015835.
- Hartmann, D. L., and M. L. Michelsen (2002a), No evidence for iris, *Bull. Am. Meteorol. Soc.*, **83**, 249–254.
- Hartmann, D. L., and M. L. Michelsen (2002b), Reply to Lindzen, Chou, and Hou comment on “No evidence for iris,” *Bull. Am. Meteorol. Soc.*, **83**, 1349–1352.
- Hartmann, D. L., J. R. Holton, and Q. Fu (2001a), The heat balance of the tropical tropopause, cirrus, and stratospheric dehydration, *Geophys. Res. Lett.*, **28**(10), 1969–1972, doi:10.1029/2000GL012833.
- Hartmann, D. L., L. A. Moy, and Q. Fu (2001b), Tropical convection and the energy balance at the top of the atmosphere, *J. Clim.*, **14**, 4495–4511.
- Kao, H.-Y., and J.-Y. Yu (2009), Contrasting eastern-Pacific and central-Pacific types of ENSO, *J. Clim.*, **22**, 615–632.
- Kley, D., J. M. Russell III, and C. Phillips (2000), SPARC assessment of upper tropospheric and stratospheric water vapour, *WCRP 133, WMO/TD 1043, SPARC Rep. 2*, 312 pp., World Clim. Res. Programme, World Meteorol. Organ., Geneva, Switzerland.
- Kuang, Z., and D. L. Hartmann (2007), Testing the fixed anvil temperature hypothesis in a cloud-resolving model, *J. Clim.*, **20**, 2051–2057.
- Kubar, T. L., D. L. Hartmann, and R. Wood (2007), Radiative and convective driving of tropical high clouds, *J. Clim.*, **20**, 5510–5526.
- Lin, B., B. A. Wielicki, L. H. Chambers, Y. X. Hu, and K.-M. Xu (2002), The iris hypothesis: A negative or positive cloud feedback?, *J. Clim.*, **15**, 3–7.
- Lin, B., B. A. Wielicki, P. Minnis, L. Chambers, K.-M. Xu, Y. Hu, and A. Fan (2006), The effect of environmental conditions on tropical convective systems observed from the TRMM satellite, *J. Clim.*, **19**, 5745–5761.
- Lindzen, R. S., M.-D. Chou, and A. Y. Hou (2001), Does the Earth have an adaptive infrared iris?, *Bull. Am. Meteorol. Soc.*, **82**, 417–432.
- Lu, J., G. Chen, and D. M. W. Frierson (2008), Response of the zonal mean atmospheric circulation to El Niño versus global warming, *J. Clim.*, **21**, 5835–5851.
- Marchand, R., T. Ackerman, M. Smyth, and W. B. Rossow (2010), A review of cloud top height and optical depth histograms from MISR, ISCCP, and MODIS, *J. Geophys. Res.*, **115**, D16206, doi:10.1029/2009JD013422.
- Miller, R. L., G. A. Schmidt, and D. T. Shindell (2006), Forced annular variations in the 20th century Intergovernmental Panel on Climate Change Fourth Assessment Report models, *J. Geophys. Res.*, **111**, D18101, doi:10.1029/2005JD006323.
- Platnick, S., M. D. King, S. A. Ackerman, W. P. Menzel, B. A. Baum, J. C. Riedi, and R. A. Frey (2003), The MODIS cloud products: Algorithms and examples from TERRA, *IEEE Trans. Geosci. Remote Sens.*, **41**, 459–473.
- Rapp, A. D., C. Kummerow, W. Berg, and B. Griffith (2005), An evaluation of the proposed mechanism of the adaptive infrared iris hypothesis using TRMM VIRS and PR measurements, *J. Clim.*, **18**, 4185–4194.
- Read, W. G., et al. (2007), Aura Microwave Limb Sounder upper tropospheric and lower stratospheric H₂O and relative humidity with respect to ice validation, *J. Geophys. Res.*, **112**, D24S35, doi:10.1029/2007JD008752.
- Rossow, W. B., and R. A. Schiffer (1999), Advances in understanding clouds from ISCCP, *Bull. Am. Meteorol. Soc.*, **80**, 2261–2287.

- Schwartz, M. J., et al. (2008), Validation of the Aura Microwave Limb Sounder temperature and geopotential height measurements, *J. Geophys. Res.*, **113**, D15S11, doi:10.1029/2007JD008783.
- Shell, K. M., J. T. Kiehl, and C. A. Shields (2008), Using the radiative kernel technique to calculate climate feedbacks in NCAR's Community Atmospheric Model, *J. Clim.*, **21**, 2269–2282.
- Soden, B. J., D. D. Turner, B. M. Lesht, and L. M. Miloshevich (2004), An analysis of satellite, radiosonde, and lidar observations of upper tropospheric water vapor from the Atmospheric Radiation Measurement Program, *J. Geophys. Res.*, **109**, D04105, doi:10.1029/2003JD003828.
- Soden, B. J., I. M. Held, R. Colman, K. M. Shell, J. T. Kiehl, and C. A. Shields (2008), Quantifying climate feedbacks using radiative kernels, *J. Clim.*, **21**, 3504–3520.
- Sohn, B.-J., and R. Bennartz (2008), Contribution of water vapor to observational estimates of longwave cloud radiative forcing, *J. Geophys. Res.*, **113**, D20107, doi:10.1029/2008JD010053.
- Stephens, G. L., et al. (2002), The CloudSat mission and the A-train: A new dimension of space-based observations of clouds and precipitation, *Bull. Am. Meteorol. Soc.*, **83**, 1771–1790.
- Su, H., et al. (2008), Variations of tropical upper tropospheric clouds with sea surface temperature and implications for radiative effects, *J. Geophys. Res.*, **113**, D10211, doi:10.1029/2007JD009624.
- Susskind, J., C. D. Barnet, and J. M. Blaisdell (2003), Retrieval of atmospheric and surface parameters from AIRS/AMSU/HSB data in the presence of clouds, *IEEE Trans. Geosci. Remote Sens.*, **41**, 390–409.
- Waters, J., et al. (2006), The Earth observing system Microwave Limb Sounder (EOS MLS) on the Aura satellite, *IEEE Trans. Geosci. Remote Sens.*, **44**, 1075–1092, doi:10.1109/TGRS.2006.873771.
- Wielicki, B. A., B. R. Barkstrom, E. F. Harrison, R. B. L. III, G. L. Smith, and J. E. Cooper (1996), Clouds and the Earth's Radiant Energy System (CERES): An Earth observing system experiment, *Bull. Am. Meteorol. Soc.*, **77**, 853–868.
- Xu, K.-M., and K. A. Emanuel (1989), Is the tropical atmosphere conditionally unstable?, *Mon. Weather Rev.*, **117**, 1471–1479.
- Xu, K.-M., T. Wong, B. A. Wielicki, L. Parker, and Z. A. Eitzen (2005), Statistical analyses of satellite cloud object data from CERES, Part I: Methodology and preliminary results of the 1998 El Niño/2000 La Niña, *J. Clim.*, **18**, 2497–2514.
- Xu, K.-M., T. Wong, B. A. Wielicki, L. Parker, B. Lin, Z. A. Eitzen, and M. Branson (2007), Statistical analyses of satellite cloud object data from CERES, Part II: Tropical convective cloud objects during 1998 El Niño and evidence for supporting the fixed anvil temperature hypothesis, *J. Clim.*, **20**, 819–842.
- Zelinka, M. D., and D. L. Hartmann (2010), Why is longwave cloud feedback positive?, *J. Geophys. Res.*, **115**, D16117, doi:10.1029/2010JD013817.
- Zhang, M. H., R. D. Cess, and S. C. Xie (1996), Relationship between cloud-radiative forcing and sea surface temperatures over the entire tropical oceans, *J. Clim.*, **9**, 1374–1384.

D. L. Hartmann, Department of Atmospheric Sciences, University of Washington, PO Box 351640, Seattle, WA 98195, USA. (dennis@atmos.washington.edu)

M. D. Zelinka, Program for Climate Model Diagnosis and Intercomparison, Lawrence Livermore National Laboratory, 7000 East Ave., L-103, Livermore, CA 94551, USA. (zelinka1@llnl.gov)